


A Modeling Investigation for Solar Flare X-Ray Stereoscopy with Solar Orbiter/STIX and Earth-orbiting Missions

Journal Article

Author(s):

Jeffrey, Natasha L.S.; Krucker, Säm; Stores, Morgan; Kontar, Eduard P.; Saint-Hilaire, Pascal; Battaglia, Andrea ; Hayes, Laura; Collier, Hannah; Veronig, Astrid; Su, Yang; Tadepalli, Srikar Paavan; Xia, Fanxiaoyu

Publication date:

2024-04-01

Permanent link:

<https://doi.org/10.3929/ethz-b-000667480>

Rights / license:

[Creative Commons Attribution 4.0 International](#)

Originally published in:

The Astrophysical Journal 964(2), <https://doi.org/10.3847/1538-4357/ad236f>



A Modeling Investigation for Solar Flare X-Ray Stereoscopy with Solar Orbiter/STIX and Earth-orbiting Missions

Natasha L. S. Jeffrey¹ , Säm Krucker^{2,3} , Morgan Stores¹ , Eduard P. Kontar⁴ , Pascal Saint-Hilaire³ , Andrea F. Battaglia^{2,5} , Laura Hayes⁶ , Hannah Collier^{2,5} , Astrid Veronig⁷ , Yang Su⁸ , Srikar Paavan Tadepalli⁹, and Fanxiaoyu Xia⁸

¹ Department of Mathematics, Physics & Electrical Engineering, Northumbria University, Newcastle upon Tyne, NE1 8ST, UK

² Institute for Data Science, University of Applied Sciences and Arts Northwestern Switzerland (FHNW), Bahnhofstrasse 6, 5210 Windisch, Switzerland

³ Space Sciences Laboratory, University of California, 7 Gauss Way, 94720 Berkeley, USA

⁴ School of Physics & Astronomy, University of Glasgow, Glasgow, G12 8QQ, UK

⁵ ETH Zürich, Rämistrasse 101, 8092 Zürich, Switzerland

⁶ European Space Agency (ESA), European Space Research and Technology Centre (ESTEC), Keplerlaan 1, NL-2201 AZ Noordwijk, The Netherlands

⁷ University of Graz, Institute of Physics & Kanzelhöhe Observatory for Solar and Environmental Research, Kanzelhöhe 19, 9521 Treffen, Austria

⁸ Purple Mountain Observatory, Chinese Academy of Sciences, Nanjing, People's Republic of China

⁹ ISRO UR Rao Satellite Center, Vimanapura, Bangalore, Karnataka—560017, India

Received 2023 December 22; revised 2024 January 26; accepted 2024 January 27; published 2024 March 27

Abstract

The Spectrometer/Telescope for Imaging X-rays (STIX) on board Solar Orbiter (SoLO) provides a unique opportunity to systematically perform stereoscopic X-ray observations of solar flares with current and upcoming X-ray missions at Earth. These observations will produce the first reliable measurements of hard X-ray (HXR) directivity in decades, providing a new diagnostic of the flare-accelerated electron angular distribution and helping to constrain the processes that accelerate electrons in flares. However, such observations must be compared to modeling, taking into account electron and X-ray transport effects and realistic plasma conditions, all of which can change the properties of the measured HXR directivity. Here, we show how HXR directivity, defined as the ratio of X-ray spectra at different spacecraft viewing angles, varies with different electron and flare properties (e.g., electron angular distribution, highest-energy electrons, and magnetic configuration), and how modeling can be used to extract these typically unknown properties from the data. Finally, we present a preliminary HXR directivity analysis of two flares, observed by the Fermi Gamma-ray Burst Monitor and SoLO/STIX, demonstrating the feasibility and challenges associated with such observations, and how HXR directivity can be extracted by comparison with the modeling presented here.

Unified Astronomy Thesaurus concepts: [The Sun \(1693\)](#); [Solar flares \(1496\)](#); [Solar x-ray flares \(1816\)](#); [Solar energetic particles \(1491\)](#); [Solar atmosphere \(1477\)](#); [Active solar corona \(1988\)](#); [Active solar chromosphere \(1980\)](#)

1. Introduction

Solar flares are a product of magnetic reconnection (e.g., Parker 1957; Sweet 1958; Priest & Forbes 2002; Su et al. 2013) in the Sun's atmosphere and the release and conversion of magnetic energy into other energies, including accelerating nonthermal charged particles (e.g., Benz 2008). Observations indicate that flares are exceptionally efficient particle accelerators, with 10%–50% of the released magnetic energy going into particle acceleration (e.g., Emslie et al. 2012; Warmuth & Mann 2016; Aschwanden et al. 2017). However, the exact mechanisms and locations of energy release and/or acceleration are not well-constrained. Competing theories of acceleration include magnetic energy dissipation by plasma waves and turbulence (Larosa & Moore 1993; Miller et al. 1996; Petrosian 2012; Vlahos et al. 2016; Kontar et al. 2017) and/or plasma instabilities and the formation of magnetic islands (Drake et al. 2006; Daughton et al. 2011; Dahlin et al. 2014) and/or shock acceleration (e.g., Chen et al. 2015).

In a standard flare model, electrons are accelerated along newly formed, closed magnetic field lines and precipitate into

the dense layers of the lower atmosphere, where they lose energy, producing hard X-rays (HXRs) (see Holman et al. 2011), while other electrons may escape into the heliosphere on open field lines, as solar energetic electrons (e.g., Krucker et al. 2007; Klein & Dalla 2017). X-rays are a direct link to flare-accelerated electrons at the Sun and a vital probe of the physical processes occurring in flares (Brown et al. 2003; Kontar et al. 2011). Over the last 20 years, the flare X-ray energy spectrum has been well observed by instruments such as the Ramaty High Energy Solar Spectroscopic Imager (RHESSI; Lin et al. 2002). However, many of the important properties required to constrain the acceleration process(es) still remain elusive, because they are difficult to determine from an X-ray spectrum viewed by a single spacecraft alone. One important property, the HXR directivity, is a vital diagnostic of the emitting, and the accelerated, electron pitch-angle distribution (often used interchangeably with electron anisotropy or directivity). The electron pitch angle is defined as the direction of electron velocity with respect to the guiding magnetic field, and thus is a key diagnostic of the dominant acceleration mechanism. As one example, accelerated electrons produced by a stochastic acceleration mechanism with efficient scattering (short timescales) are expected to produce isotropic pitch-angle distributions (although, isotropy is usually prescribed in such models to increase acceleration efficiency) (e.g., Melrose 1994; Miller et al. 1996; Petrosian 2012). Moreover, processes such

as resonant scattering due to waves propagating parallel to the magnetic field may preferentially scatter at 90° (e.g., Petrosian & Donaghy 1999). In order to understand HXR directivity, we must also take into account electron transport effects in the solar plasma that broaden the electron distribution, increasing the isotropy by, e.g., collisional (Jeffrey et al. 2014; Kontar et al. 2015, 2019) and/or non-collisional pitch-angle scattering (Kontar et al. 2014; Musset et al. 2018). Thus, even if the accelerated distribution is strongly beamed, the angular distribution of radiating electrons is expected to isotropize as they are transported from the corona to the chromosphere, where the bulk of HXRs are produced and observed, due to the bremsstrahlung dependency on density.

Due to different issues, HXR directivity has been difficult to routinely measure to date. We have sought to measure the HXR and electron directivity in several different ways: (1) HXR albedo mirror analysis of strong solar flares (Bai & Ramaty 1978; Kontar & Brown 2006). Novel but limited albedo mirror (X-ray Compton backscattering in the photosphere) analyses suggests that the HXR emitting electron distribution is close to isotropic especially below 150 keV, at least for the few events published (Dickson & Kontar 2013). (2) Using statistical flare studies of center-to-limb variations in, e.g., flux or spectral index. Statistical studies such as Kašparová et al. (2007) studied 398 flares but gave no clear conclusion regarding average flare directivity, particularly because the study was only able to investigate in the (mainly thermal) 15–20 keV range. (3) Using linear X-ray polarization measurements from a single flare with one satellite (e.g., Tindo et al. 1970; McConnell et al. 2004). There is a direct link between X-ray linear polarization and electron anisotropy (Bai & Ramaty 1978; Leach & Petrosian 1983; Jeffrey & Kontar 2011; Jeffrey et al. 2020). Nevertheless, observations with past instruments and nondedicated polarimeters (e.g., RHESSI), have proved problematic, owing to instrumental issues, although rare RHESSI observations suggested some level of directivity (e.g., Suarez-Garcia et al. 2006). Currently, there is no solar-dedicated X-ray polarimeter to measure directivity, but the Polarization and Directivity X-Ray Experiment (PADRE; a CubeSat planned to be launched in 2025)¹⁰ will be capable of X-ray spectropolarimetry up to ≈ 100 keV. (4) By simultaneously observing a single flare with two satellites at different viewing angles (i.e., measuring HXR directivity). Previous stereoscopic studies (e.g., Kane et al. 1992, 1998) found no clear evidence for directivity at X-ray energies between 25 and 125 keV. However, such observations can suffer from calibration issues, making the results unreliable. Thus, it is fundamental that the two instruments have a well-known energy cross-calibration before any data is interpreted. Further, previous stereoscopic studies did not take effects such as X-ray albedo into account. Now, with the successful deployment of Solar Orbiter (SoIo; Müller et al. 2020) and its Spectrometer/Telescope for Imaging X-rays (STIX; Krucker et al. 2020), we are now able to detect flares with different viewing angles from the Earth–Sun line as close as 0.28 au (at perihelion) and up to inclinations of $\approx 25^\circ$. Here, we perform modeling that can be compared directly with stereoscopic observations from SoIo/STIX and current or near-future Earth-orbiting missions such as the Gamma-ray Burst Monitor (GBM) on board Fermi (Meegan et al. 2009), Advanced Space-based Solar

Observatory/Hard X-ray Imager (ASO-S/HXI; Krucker et al. 2019; Su et al. 2019; Zhang et al. 2019), Aditya-HELIOS, PADRE, and beyond, acting as a foundation for extracting the electron directivity and other electron and flare properties from stereoscopic observations. Section 2 provides an overview of the preliminary modeling. Section 3 displays and discusses a selection of modeling results, showing how certain electron and flare parameters can be extracted from HXR stereoscopy. A preliminary analysis of HXR directivity from two flares observed by SoIo/STIX and Fermi/GBM is shown in Section 4. Section 5 summarizes the main results of this study.

2. Models of HXR Directivity

2.1. Coronal Transport-dependent Modeling

Following previous works (Jeffrey et al. 2014, 2019; Kontar et al. 2015; Stores et al. 2023), the evolution of an electron flux F in energy E [erg], cosine of the pitch angle (β), $\mu = \cos \beta$, and distance along the guiding magnetic field z [cm], from a coronal loop apex to the chromosphere can be modeled using a time-independent Fokker–Planck equation (see Equation (1)). This takes into account the processes that alter electron properties, including their directivity, e.g., Coulomb collisions (represented by the last two terms on the right-hand side (rhs) of Equation (1)) and turbulent scattering (represented by the first term on the rhs of Equation (1)) from magnetic fluctuations using a diffusion coefficient $D_{\mu\mu}$, often chosen to be isotropic for simplicity, i.e., as shown by Jeffrey et al. (2020):

$$\begin{aligned} \mu \frac{\partial F}{\partial z} = & \underbrace{\sqrt{\frac{m_e}{2E}} \left\{ \frac{\partial}{\partial \mu} \left[D_{\mu\mu}(\mu, z) \frac{\partial F}{\partial \mu} \right] \right\}}_{\text{turbulent scattering}} \\ & + \underbrace{\Gamma m_e^2 \left\{ \frac{\partial}{\partial E} \left[G(u[E]) \frac{\partial F}{\partial E} + \frac{G(u[E])}{E} \left(\frac{E}{k_B T} - 1 \right) F \right] \right\}}_{\text{collisional energy losses}} \\ & + \underbrace{\frac{\Gamma m_e^2}{8E^2} \left\{ \frac{\partial}{\partial \mu} \left[(1 - \mu^2) [\text{erf}(u[E]) - G(u[E])] \frac{\partial F}{\partial \mu} \right] \right\}}_{\text{collisional pitch-angle scattering}}, \end{aligned} \quad (1)$$

where $\Gamma = 4\pi e^4 \ln \Lambda n / m_e^2$, for electron charge e [statC], Coulomb logarithm $\ln \Lambda$, electron mass m_e [g], and coronal number density n [cm⁻³]. The error function is given by $\text{erf}(u)$ and $G(u) = (\text{erf}(u) - u \text{erf}'(u)) / 2u^2$, where u is the dimensionless velocity $u = v / (\sqrt{2} v_{\text{th}})$, v is the velocity [cm s⁻¹], $v_{\text{th}} = \sqrt{k_B T / m_e}$ [cm s⁻¹] for Boltzmann constant k_B and coronal temperature T , and $\text{erf}'(u) = \frac{d \text{erf}}{du}$. Such functions control the lower-energy ($E \approx k_B T$) electron interactions, ensuring that they become indistinguishable from the background thermal plasma.

To allow the evolution of an electron distribution to be modeled in space, energy, and pitch angle to the guiding magnetic field, Equation (1) can be solved numerically by its conversion into a set of time-independent stochastic differential equations (e.g., Gardiner 1986; Strauss & Effenberger 2017) for E , μ , and z .

¹⁰ <https://padre.ssl.berkeley.edu/>

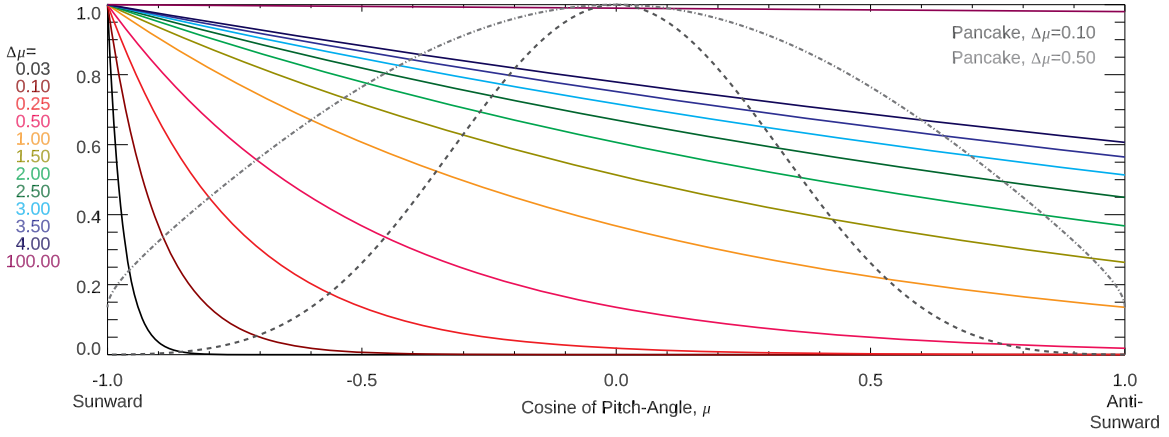


Figure 1. Examples of beamed to isotropic electron directivity (pitch-angle distribution) controlled by the parameter $\Delta\mu$ in Equation (2). Here, small values of $\Delta\mu$ produce highly beamed distributions, with the bulk of the electron populations moving sunward while large values of $\Delta\mu$ produce closer to isotropic distributions. The gray dashed and dashed-dotted lines also show two “pancake” distribution examples (Equation (3)) with $\Delta\mu = 0.1$ and $\Delta\mu = 0.5$ where a high fraction of the electrons are directed at an angle of 90° to the guiding magnetic field, resulting in a pitch-angle distribution that may be more suitable for certain mechanisms.

2.2. Transport-independent Modeling

For a simple comparison and for a basic understanding of the expected results, we also perform transport-dependent simulations (similar to Jeffrey & Kontar 2011), where a chosen electron flux $F(E, \mu)$ is deposited into the chromosphere and is modeled using

$$F(E, \mu) \propto E^{-\delta_{\text{FP}}} \exp\left(-\frac{(1 + \mu)}{\Delta\mu}\right). \quad (2)$$

This function uses a single parameter $\Delta\mu$ to alter the electron directivity from beamed to isotropic, where large values of $\Delta\mu$ ($\gg 1$) produce isotropic distributions and small values of $\Delta\mu$ ($\ll 1$) produce field-aligned “beamed” distributions (Figure 1). Here, the electron spectral index δ_{FP} is the spectral index related to the footpoint emission assuming a thick-target chromosphere (not the injected or accelerated power-law index). Again, for this parameter study, we assume the electron properties remain identical at all emitted pitch angles $\mu = \cos\beta$.

It is also interesting to consider a “pancake” directivity (where the bulk of the emitting electrons have their velocity directed at 90° to the guiding magnetic field, see Figure 1) using

$$F(E, \mu) \propto E^{-\delta_{\text{FP}}} \exp\left(-\frac{(1 - \sqrt{1 - \mu^2})}{\Delta\mu}\right). \quad (3)$$

While solar models usually invoke isotropic turbulence as accelerator and/or scatterer (because the form of the turbulence is unconstrained), solar wind studies, guided by in situ measurement, show anisotropy with field fluctuations greater in the direction perpendicular to the field (i.e., $\delta B_\perp > \delta B_\parallel$); see, e.g., Alexandrova et al. (2013).

In all modeling scenarios, the resulting X-ray bremsstrahlung distribution is calculated using the full polarization angle-dependent bremsstrahlung cross section (Gluckstern & Hull 1953; Haug 1972), using the forms of Emslie et al. (2008) and Jeffrey & Kontar (2011).

Finally, the photospheric “backscattered” X-ray albedo component, which is critical for the correct determination of the HXR directivity (Figure 3), is modeled using the Monte

Carlo albedo code of Jeffrey & Kontar (2011). The albedo X-rays are viewed alongside those X-rays directly emitted from the HXR source, which are often called the primary X-rays. The albedo component consists of energy and pitch-angle altered photons, and it creates a “bump” in the X-ray spectrum over the energies of 10–100 keV with a peak around the 20–50 keV range (see Figure 3). An isotropic HXR source produces the minimum albedo, and even its flux can account for up to 40% of the detected flux in the peak albedo energy range between 20 and 50 keV (e.g., Bai & Ramaty 1978; Kontar & Brown 2006; Kašparová et al. 2007).

The full X-ray distribution (direct primary emission from the chromosphere plus the photospheric albedo component) is examined for various spacecraft viewing angles. We do not perform an exhaustive parameter study here; rather, we set the height of all chromospheric emission to $h = 1$ Mm when calculating the X-ray albedo component.

2.3. Measuring the HXR Directivity

Any flare location on the solar disk (or the flare viewing angle) can be defined by its radial position given by $\sqrt{x^2 + y^2}$ using the local flare (x, y) coordinates (with the corresponding solar center viewed by each spacecraft defined as $[x = 0, y = 0]$.) The heliocentric angle is measured in the plane of the spacecraft, the flare, and the solar center (this plane can differ for each spacecraft), given by $\theta = \arcsin(\sqrt{x^2 + y^2}/R_\odot)$ where R_\odot is the solar radius for each spacecraft observation. An example of a flare observed at two heliocentric angles by two different spacecraft is shown in Figure 2, panel (a).

In all simulations (similar to X-ray observations), a heliocentric angle of $\theta = 0^\circ$ corresponds to the spacecraft viewing the flare at the disk center, while $\theta = 90^\circ$ corresponds to viewing the flare at the solar limb. Here, HXR directivity is defined as the energy-dependent ratio,

$$\text{HXR directivity} = \frac{\text{HXR flux at spacecraft 1, small } \theta}{\text{HXR flux at spacecraft 2, large } \theta}, \quad (4)$$

i.e., the ratio of X-ray energy spectra (see Figure 3), where we define spacecraft 1 (SC1) as the spacecraft viewing the flare at a smaller heliocentric (observer) angle θ and spacecraft 2 (SC2) as the spacecraft viewing the flare at a larger angle θ . We do

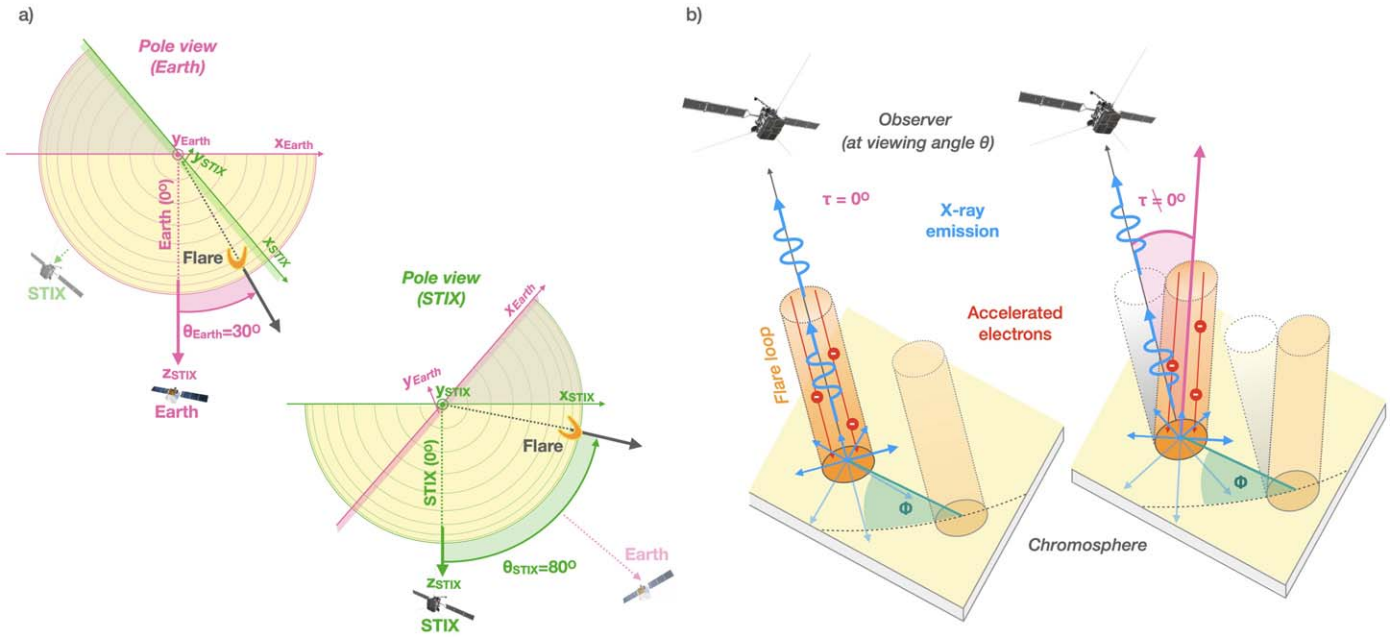


Figure 2. (a) Example of a flare, observed by two different spacecraft, at two different heliocentric (viewing) angles: θ_{Earth} viewed by spacecraft at Earth, and θ_{STIX} viewed by STIX. Locally, the heliocentric angle is measured in the plane of the spacecraft, the flare, and the solar center (which can differ for each spacecraft), given by $\theta = \arcsin(\sqrt{x^2 + y^2}/R_\odot)$, i.e., the x and y axes are defined relative to the observer position, as shown. (b) Locally, the flare can also be tilted with respect to the local solar radial direction (Emslie et al. 2008). This tilt is represented by τ , where $\tau = 0^\circ$ represents a scenario where the flaring loop apex is aligned with the local solar radial direction. The effect of τ on HXR directivity is also dependent on Φ , the azimuthal direction of the axis around which the loop is tilted (Emslie et al. 2008).

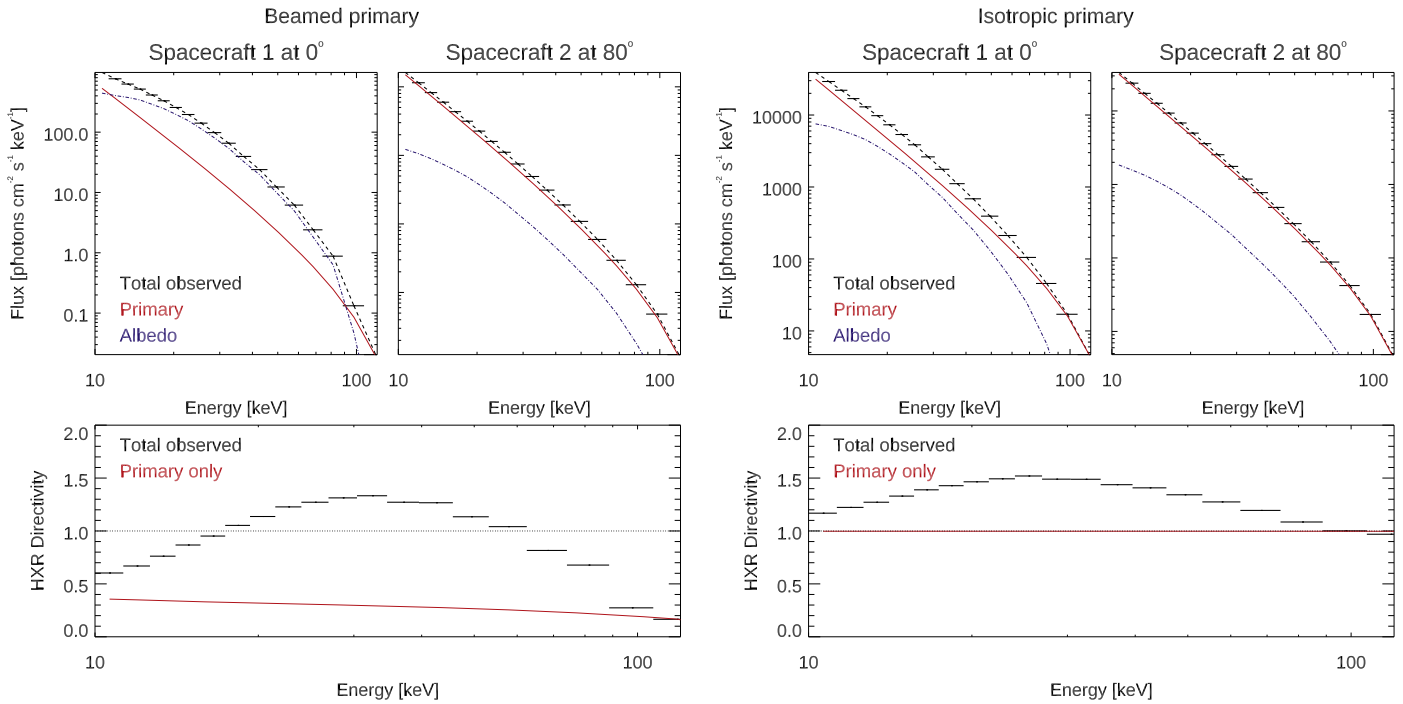


Figure 3. Top row: Examples of model spectra (black indicates total observed X-ray emission) and individual components (red indicates primary X-ray emission and blue is for albedo X-ray emission) for a flare with a beamed (toward the solar surface) electron directivity (left) and an isotropic electron directivity (right). In each case, the spectra are observed at two different spacecraft viewing angles of 0° (disk center) and 80° (close to the limb). Bottom row: Resulting HXR directivity (black indicates total observed emission and red is for primary emission only) found from the ratio of spectra for the beamed (left) and isotropic (right) cases. These examples show the importance of accounting for the X-ray albedo component, which is greatest at the disk center and smallest at the limb, while increasing for greater downward directivity.

this for consistency, as the X-ray albedo component is always greatest near the disk center (at small viewing angles), which leads to >1 directivity ratios at energies where the X-ray albedo is found, i.e., $\approx 20\text{--}90$ keV.

We also consider the local geometry via the loop tilt τ (in Figure 2, panel (b)). Following Emslie et al. (2008), the loop tilt is defined as the angle between the line connecting the loop apex and the local solar radial direction. When a closed

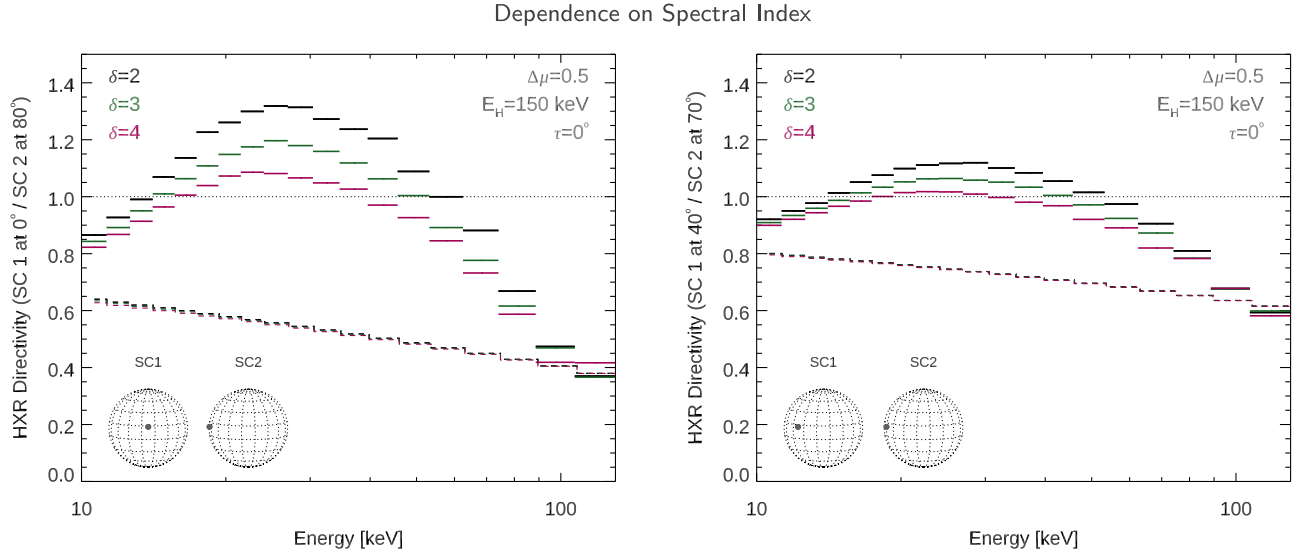


Figure 4. HXR directivity (ratio of HXR spectra) for spacecraft viewing angles of 0° and 80° (left) and 40° and 70° (right), showing how the directivity can change with the power-law spectral index of the electron spectrum (using $\delta \equiv \delta_{\text{FP}} = 2, 3, 4$ (footpoint)). In these examples, we use an electron anisotropy of $\Delta\mu = 0.5$, an electron high-energy cutoff of $E_H = 150$ keV, and a loop tilt of $\tau = 0^\circ$. Solid bars: Total observed flux ratio. Dashed lines: Primary component only, without albedo.

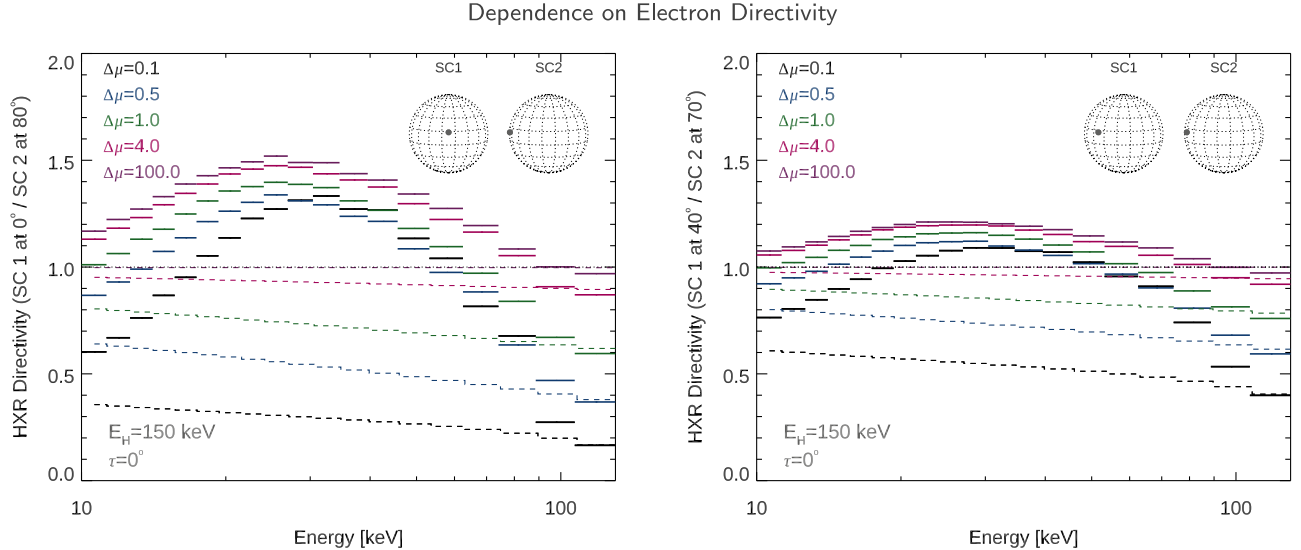


Figure 5. HXR directivity for spacecraft viewing angles of 0° and 80° (left) and 40° and 70° (right), showing how the HXR directivity changes with the directivity of the electron distribution (from very beamed $\Delta\mu = 0.1$ to isotropic $\Delta\mu = 100.0$). In these examples, we use an electron spectral index of $\delta_{\text{FP}} = 2$ (footpoint), an electron high-energy cutoff of $E_H = 150$ keV, and a loop tilt of $\tau = 0^\circ$. Solid bars: Total observed flux ratio. Dashed lines: Primary component only, without albedo.

flare loop is viewed side-on, $\tau = 0^\circ$ if the loop apex sits directly along the local solar radial direction. In Emslie et al. (2008), it was shown that loops with tilt $\tau > 0^\circ$ produce a polarization angle $\Psi > 0^\circ$, and here we examine how τ affects the HXR directivity from stereoscopic observations. τ is an important parameter, as it can help us to constrain the local magnetic geometry of the flare (or at least the average, dominant geometry in a flare with a complicated magnetic geometry).

3. Selection of Modeling Results

All the results here are shown for spatially integrated X-ray emission. Although STIX has imaging capabilities, it is likely that we will not have spatially resolved spectra from the second spacecraft viewing the flare (e.g., Fermi/GBM or PADRE).

3.1. Effects of HXR Albedo and Chosen Parameters of Study

Figures 3–7 all show the effects of the X-ray albedo component and why it is so essential to account for this X-ray component before determining the HXR directivity and extracting electron and flare properties.

In general, the albedo component acts to increase the flux in small observer viewing angles, changing the HXR directivity ratio at energies between 10 and 100 keV from <1 (no albedo and assuming downward electron beaming) to >1 (with albedo). As already described, albedo is largest at smaller heliocentric angles. Flares with greater sunward directivity will produce a larger albedo fraction compared to isotropic distributions (e.g., Jeffrey & Kontar 2011).

Flatter electron energy spectra (i.e., smaller spectral indices δ_{FP}) lead to higher albedo percentages and hence larger HXR directivity ratios over the ~ 20 – 70 keV range (Figure 4). The

Dependence on Electron High Energy Cutoff

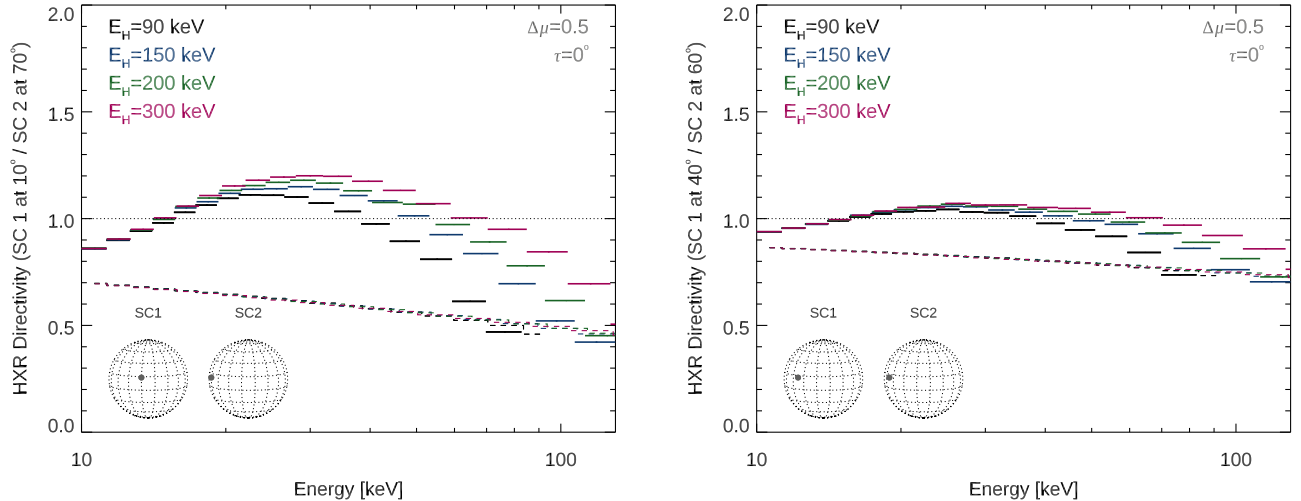


Figure 6. HXR directivity for spacecraft viewing angles of 10° and 70° (left) and 40° and 60° (right), showing how the HXR directivity changes with the electron high-energy cutoff (from $E_H = 90$ keV to $E_H = 300$ keV). In these examples, we use an electron spectral index of $\delta_{\text{FP}} = 2$ (footpoint), an electron directivity of $\Delta\mu = 0.5$, and a loop tilt of $\tau = 0^\circ$. Solid bars: Total observed flux ratio. Dashed lines: Primary component only, without albedo.

spectral index is a prime example of a nonthermal electron parameter that can be routinely extracted from single viewing angle spectral data and hence constrained before comparison with simulation.

Therefore, alongside the determination of electron directivity, we concentrate on examining parameters not easily constrained by current (single viewing angle) observations, such as the

1. Electron high-energy cutoff E_H , which is related to the highest-energy accelerated electrons and hence also the properties of the acceleration mechanism and location; as well as the
2. Loop tilt τ related to the local magnetic geometry.

In the majority of study cases, unless different properties are explicitly stated for that case, the following properties are used: $\Delta\mu = 0.5$ (see Figure 1), $E_H = 150$ keV, $\tau = 0^\circ$, and $\delta_{\text{FP}} = 2$ (footpoint).

3.2. Electron Directivity

Here, we test five different electron footpoint directivities (see Figure 5), going from completely isotropic ($\Delta\mu = 100$) to very beamed ($\Delta\mu = 0.1$). Figure 5 shows the resulting HXR directivities for spacecraft viewing angles of (left) SC1 at 0° and SC2 at 80° , and (right) SC1 at 40° and SC2 at 70° . While isotropic distributions produce the highest values of HXR directivity (due to albedo) over the 20–50 keV range, very beamed distributions show the greatest HXR directivity change over the energy range of 10–100 keV (comparing the dashed and solid lines), due to the larger albedo fraction produced by a large sunward directivity. At the curve peak (over the 20–50 keV range), the difference between each directivity curve (beamed to isotropic) is at a minimum. At higher energies above 50 keV, the albedo dominance starts to diminish and the HXR directivity curve tends back to what we expect to see without the effects of albedo (dashed lines). Such trends stress the importance of using the entire observed X-ray energy range for the determination of electron directivity. A comparison of the left and right panels in Figure 5 demonstrates

how the HXR directivity curves change for different spacecraft viewing angles. In general, larger differences in spacecraft viewing angles are preferable because they show the greatest difference between different electron directivities over all energies. However, Figure 5 (right) demonstrates that even small differences in viewing angles (in this case 40° and 70°) can still be used to extract the electron directivity, in particular if the flux uncertainties are small (large flare) and the whole energy range is used (this is discussed in Section 3.6).

In Figure 8, we investigate the pancake distribution, where the peak electron flux is directed at 90° to the guiding magnetic field. Interestingly, a directed pancake distribution (using $\Delta\mu = 0.5$, see Figure 1) can produce an HXR directivity spectrum comparable to a completely isotropic distribution, differing at the highest energies (≥ 80 keV) only.

3.3. High-energy Cutoff

As discussed, the HXR directivity curves are also sensitive to the “high-energy cutoff” E_H . Figure 6 demonstrates how the HXR directivity changes for four different high-energy cutoff values of $E_H = 90, 150, 200,$ and 300 keV, and each curve is different above 20 keV (in a real flare, it is likely that the isotropic thermal distribution will also dominate at ≤ 20 keV, giving a directivity close to 1). The greater the value of E_H , the flatter (or larger) the HXR directivity remains up until higher energies. When E_H is lower, the lack of higher-energy electrons creates an X-ray deficit in the 20–100 keV energy range.

In Figure 6, we also compare the spacecraft observing angles of (left) SC1 at 10° and SC2 at 70° , and (right) SC1 at 40° and SC2 at 60° . Although the curves overlap at lower energies (≤ 30 keV), individual curves are distinguishable even for the small differences in viewing angle (20° , right). However, for real data, such distinctions will be highly dependent on the measurement uncertainties for the individual events.

3.4. Loop Tilt, Footpoint Orientation, and Magnetic Field Geometry

In Figure 7 (top row), we show an example of how the tilt of the flare loop (dominant magnetic field direction) can change

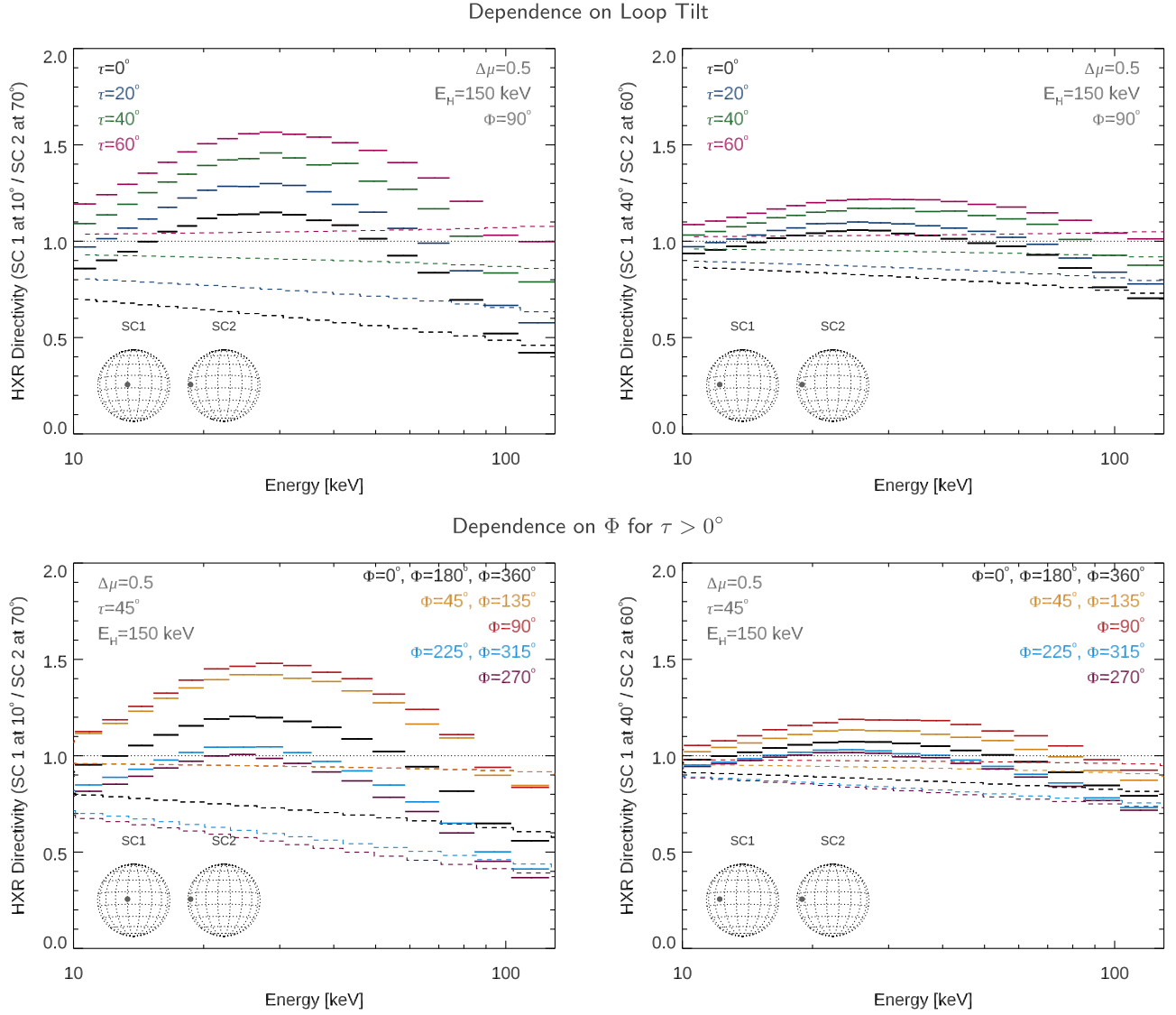


Figure 7. Top row: HXR directivity for spacecraft viewing angles of 10° and 70° (left) and 40° and 60° (right), showing how the HXR directivity changes with tilt of the magnetic loop away from the local solar radial direction (from $\tau = 0^\circ$ to $\tau = 60^\circ$). In these examples, we use an electron spectral index of $\delta_{\text{FP}} = 2$ (footpoint), an electron directivity of $\Delta\mu = 0.5$, an electron high-energy cutoff of $E_H = 150$ keV and $\Phi = 90^\circ$. Solid bars: Total observed flux ratio. Dashed lines: Primary component only, without albedo. Bottom row: An example of how the HXR directivity can change at values of $\tau > 0^\circ$ (here $\tau = 45^\circ$) with Φ , the azimuthal direction of the axis around which the loop is tilted (Emslie et al. 2008).

the HXR directivity curves. For this example, we pick a high-energy cutoff value of 150 keV, a footpoint anisotropy of $\Delta\mu = 0.5$ (mildly beamed), and spacecraft viewing angles of 10° and 70° (left) and 40° and 60° (right).

Figure 7 (top row) shows the HXR directivity curves for four different loop tilts of $\tau = 0^\circ$, 20° , 40° , and 60° . As the loop tilts, the direction of the X-ray emission with respect to the observer changes. From Figure 7, we can see that increasing the loop tilt τ has the effect of shifting the entire HXR directivity curve up to higher values.

The effect of the loop tilt is not only dependent on the heliocentric angle θ but on Φ , the azimuthal direction of the axis around which the loop is tilted (Emslie et al. 2008) (azimuth of the footpoint line relative to the radial line; see Figure 2, panel (b)). In Figure 7 (top row) and all other simulations shown in this paper, $\Phi = 90^\circ$, which corresponds to a loop with footpoints oriented perpendicular to the direction from the disk center to the flare location.

Φ is similar to θ , in the sense that it should be observable and hence able to be constrained using STIX and/or EUV imaging observations. Once θ and Φ are determined, directivity can be associated with the local magnetic loop configuration.

An example of how the HXR directivity can vary, using $\tau = 45^\circ$, with different Φ ranging from 0° to $0^\circ = 360^\circ$ is shown in Figure 7 (bottom row). Values of $\Phi < 90^\circ$ and $\Phi > 90^\circ$ produce an overall lower HXR directivity at all values of energy.

Determination of the loop tilt is useful, since properties regarding the magnetic configuration are often difficult to constrain from imaging alone. This result matches the work of Emslie et al. (2008), showing how the polarization angle (which will be measurable with PADRE) can also be used to determine the orientation of the loop.

In real observations, this property may be complicated by multiple loops tilted at different angles. Here, we are only interested in spatially integrated flare observations matching the

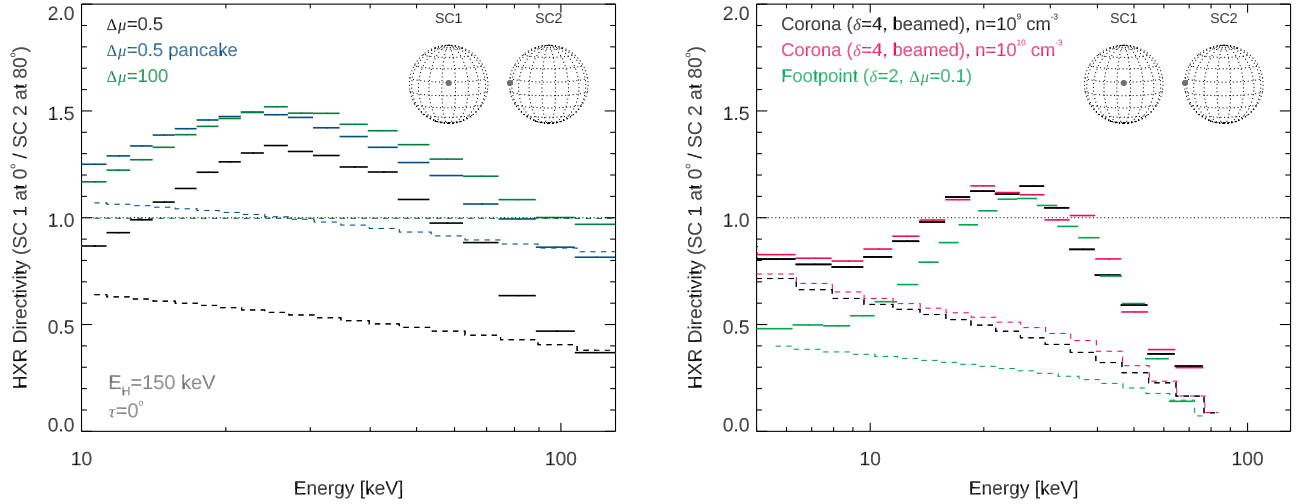


Figure 8. (Left) Comparison of the HXR directivity for a downward beamed ($\Delta\mu = 0.5$) distribution, an isotropic distribution, and a pancake distribution with the bulk of the electron velocity directed toward 90° . It is interesting to note that the HXR directivity curve from a pancake distribution can appear similar to an isotropic distribution. (Right) Effects of collisions in coronal plasma of different densities using densities of $n = 10^9$ cm $^{-3}$ and $n = 10^{10}$ cm $^{-3}$. For the coronal injected cases, $\delta = 4$ refers to the injected electron spectral index (black and pink), while for the footpoint case $\delta = 2 = \delta_{FP}$, the spectral index of the emitting electron distribution in the chromosphere.

current capabilities of (most) instruments, and hence the tilt parameter will indicate an overall average loop tilt configuration.

3.5. Coronal Transport Effects: A Brief Discussion

Transport effects such as collisions and turbulent scattering act to diminish directivity; collisions tend to remove directivity at lower energies, while turbulent scattering can isotropize and remove directivity efficiently at higher electron energies, leading to completely isotropic distributions, as shown for X-ray polarization in Jeffrey et al. (2020).

The inclusion of a background thermal component in flare X-ray spectra will also tend to hide any directivity signatures at lower energies below 20 keV, because it is expected the thermal component will have a directivity close to isotropic. Other transport effects such as electron-beam-induced return currents (e.g., Knight & Sturrock 1977; Emslie 1980; Zharkova & Gordovskyy 2006; Alaoui & Holman 2017; Alaoui et al. 2021) may also play a role, but we do not attempt an exhaustive coronal transport study in this initial work.

As one example, we demonstrate the effects of coronal collisions using two simulation runs. The electron distribution is injected into a coronal loop apex as a power law with $\delta = 4$ (corona), giving $\delta_{FP} \approx 2$ (footpoint). In the corona, we model collisional transport using a background temperature of $T = 20$ MK, and a half-loop length $L = 20''$ (as seen from Earth, from the apex to chromosphere). Two values of coronal number density are used: $n = 10^9$ cm $^{-3}$ and $n = 10^{10}$ cm $^{-3}$.

The resulting HXR directivity curves are compared in Figure 8 (right). We compare the curves with a transport-dependent footpoint simulation using the following parameters: $\delta_{FP} = 2$ (footpoint), $\Delta\mu = 0.1$, $E_H = 90$ keV, and $\tau = 0^\circ$. Here, we can clearly see that the transported electron distribution (black and pink curves) isotropize as expected, in particular at lower energies < 30 keV, increasing the value of the primary (dashed lines) and total (solid bars) HXR directivity, compared to the resulting (similar) HXR directivity created by the electron distribution injected at the footpoint (green).

3.6. Effect of Uncertainties

In order to account for the uncertainties associated with real X-ray data and the limits of HXR directivity determination, we examine two simple examples in Figure 9 where the individual spectra are assigned random flux uncertainties with a maximum of either 5% or 10%.

For small differences in viewing angle ($\approx 20^\circ$), at high heliocentric angles ($> 40^\circ$), large uncertainties ($\approx 10\%$) would obscure the directivity, but 5% uncertainties could allow differences at low (10–20 keV) and higher energies (> 80 keV) to show, allowing the observer to extract whether the distribution is isotropic or has some level of directivity at the very least.

For large differences in viewing angles, 5% uncertainties should allow the directivity to be constrained to a greater degree, while 10% should allow us to distinguish between “beamed” and “isotropic” electron anisotropies.

The errors in the observed X-ray fluxes have three main contributing factors: counting statistics, the accuracy of the pre-flare background subtraction, and systematic errors in the calibration of the instrument. In the low-energy range where the signal strength is high and well above the background level, systematic errors dominate the total errors in the flux. By comparing flare observations with similar viewing angles, the bias of systematic errors can be evaluated. In Section 4, we show that systematic errors between STIX and FERMI/GBM are around 6% for our preliminary analysis of a single event. As the observed HXR spectra are steep, fluxes at higher energies are much weaker and eventually become of similar strength or even below the pre-flare background level. Hence, for high energies, the error is given by a combination of counting statistics and/or the accuracy of the background subtraction. In practice, this leads to an upper limit on the photon energy for which errors stay below a scientifically meaning value.

4. Preliminary Comparison with HXR Data

While it appears to be straightforward to determine X-ray directivity by measuring two absolute fluxes from two different

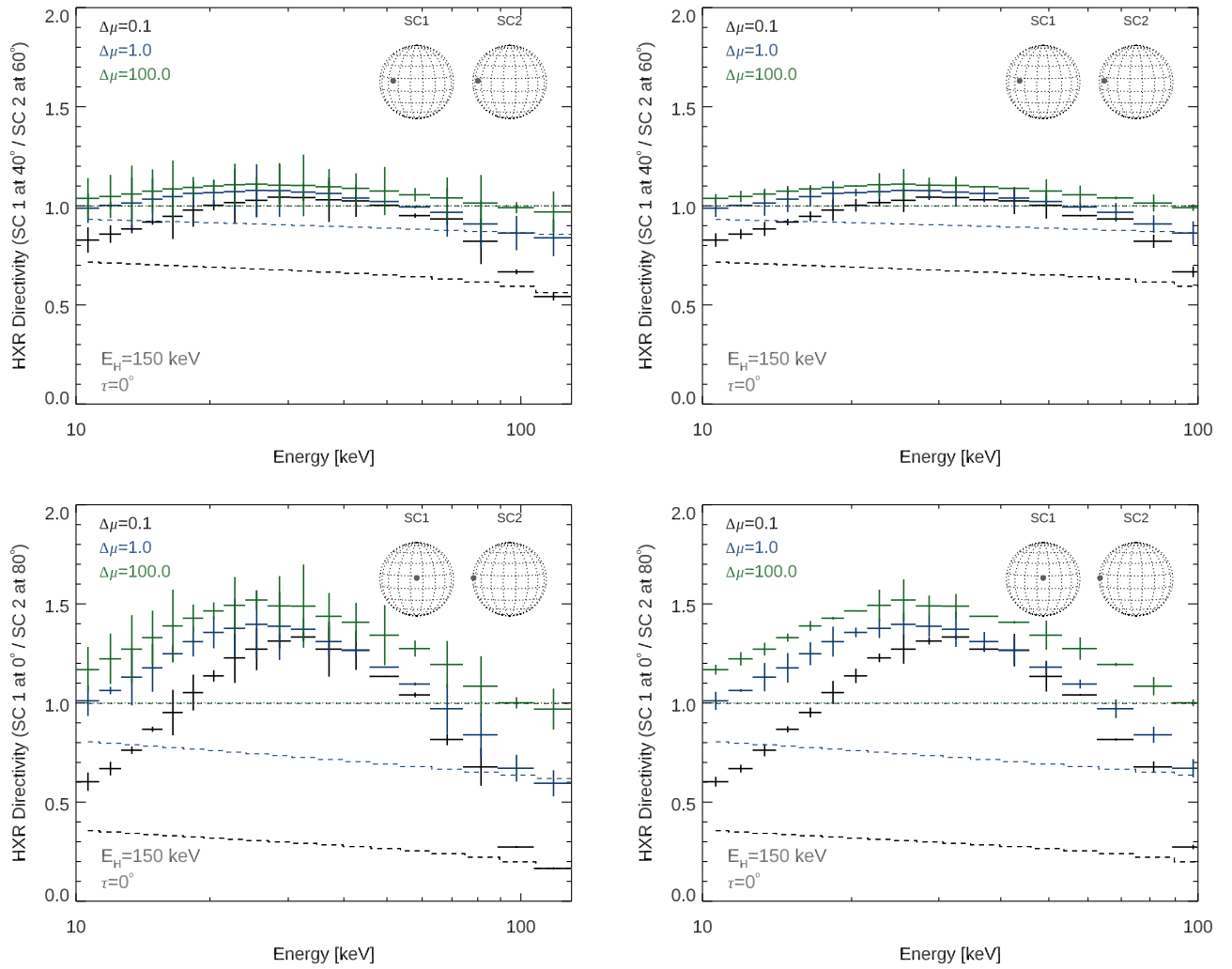


Figure 9. Top row: HXR directivity curves for small-difference viewing angles of 40° and 60° , created from individual simulated spectra using random uncertainties with a maximum of (a) 10% and (b) 5% in all energy bins. Bottom row: Same as top, but for large-difference viewing angles of 0° and 80° .

vantage points, the difficulty of establishing an accurate absolute flux calibration in X-rays makes directivity measurement extremely challenging. To illustrate the difficulty of absolute X-ray calibration, a published comparison of X-ray instrumentation can be consulted. Kirsch et al. (2005) compared Crab Nebula observations by many different astrophysical X-ray observatories and found that deviations of 10% are frequently seen. For solar observations, the same difficulties remain, although we have two strong methods to check the validity of the absolute flux calibration: (1) thermal X-ray emission, which is typically seen below 20 keV, is expected to be isotropic, at least within our targeted goal of a few percent accuracy in the absolute flux measurement. Hence, the measured directivity of the thermal emission should be unity within the achieved accuracy, and (2) as a control group, we can use flares for which the viewing angles are similar for two spacecraft. Each time *Solo* is crossing the Earth–Sun line, we will get a few days where the look direction is similar to Earth-orbiting observatories. Alternatively, we can select flares which occur at angles in between the two spacecraft. As the Fermi/GBM calibration is less accurate in the thermal energy range compared to the nonthermal range, here we will use the second approach. Despite having these consistency checks, the

initial step is to do the best possible calibration with an accurate measurement of the associated errors.

STIX has reached a satisfactory calibration level for most science topics. For directivity studies, we must implement a few further corrections and then publish the results including their accuracy. This includes, for example, the “fuzziness” of the STIX grids as a function of photon energy. Currently, the grids are assumed to have perfectly sharp edges, which is obviously a simplification. As the fine tuning of the STIX calibration is ongoing, here we show initial results with the currently available accuracy of the absolute flux calibration. These results give insight regarding what we observe within the currently available calibration, but they should not yet be used to draw stringent quantitative conclusions on electron beaming. What we present in this section should therefore be seen as an outlook on future directivity results. In Figure 11, we show the HXR directivity curves for two flares, one for which the flare is seen from a very similar look direction (SOL2021-11-01T01), and a second one for which the viewing angle is separated by $\sim 30^\circ$ (SOL2021-08-28T05). As we only intend to show that such observations are feasible without drawing quantitative conclusions, we will not discuss the details of each flare in this paper.

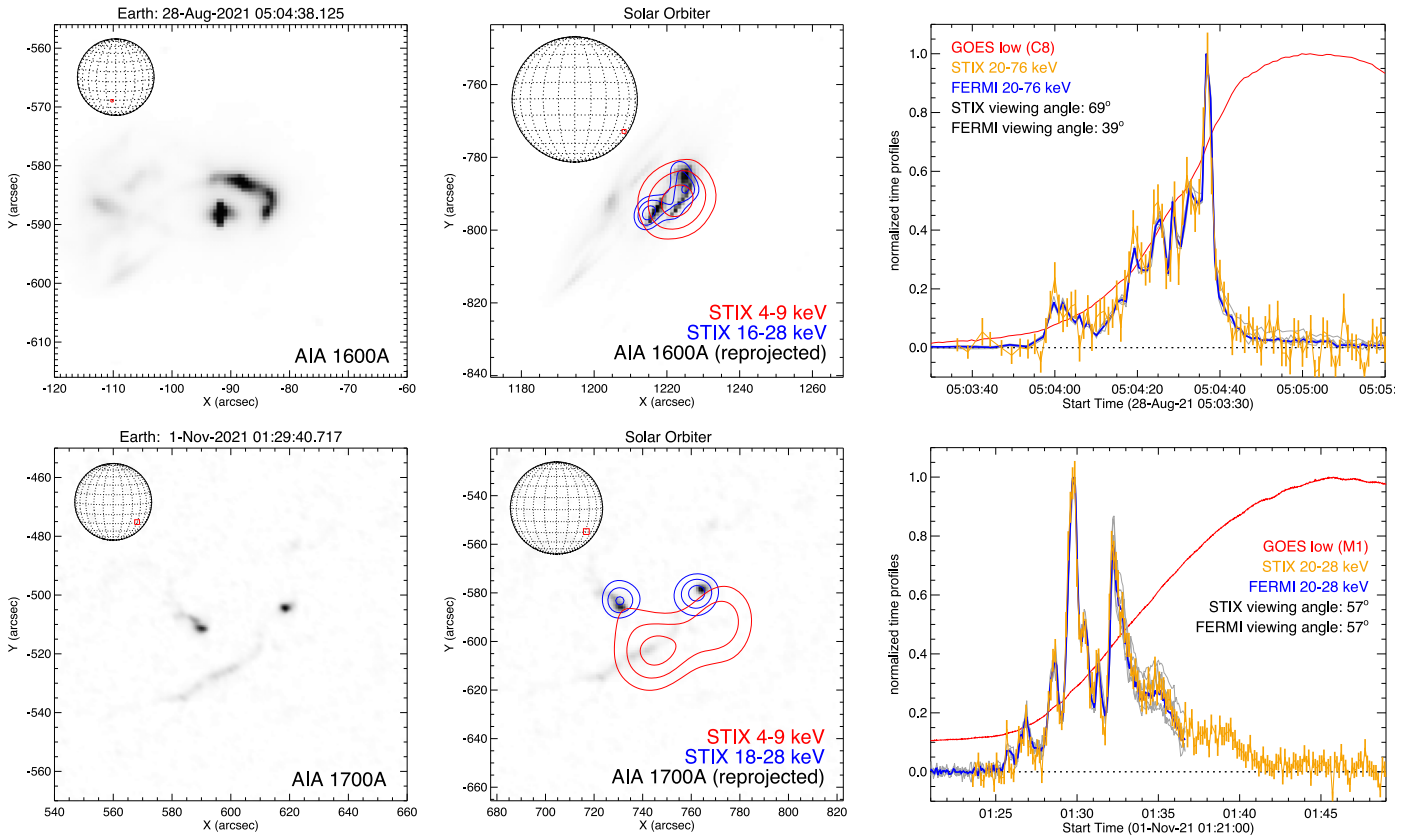


Figure 10. X-ray images and time profiles of the two selected flares: (Top) Flare SOL2021-08-28T05, where STIX and Fermi/GBM have clearly different viewing angles. (Bottom) Flare SOL2021-11-01T01 is seen from essentially the same viewing angle for both instruments. The images show the Solar Dynamics Observatory Atmospheric Imaging Assembly (SDO/AIA; Lemen et al. 2012) UV source configuration as seen from Earth (left), as well as reprojected to the SoLO vantage points (center). Both flares show a good spatial match between the chromospheric UV emission and the nonthermal HXR signal. On the right, time profiles are shown. All curves are normalized to their maximum and therefore the directivity signal is not obvious in these overview figures. The STIX profiles have been shifted to account for the different light travel time to SoLO. The individual Fermi/GBM detectors are shown in light gray and the detector-summed curve is shown in blue. The individual Fermi/GBM detectors give similar profiles, except for the last part of the November 1 flare (SOL2021-11-01T01). This could possibly be an effect of pileup. For STIX, the profiles have been produced by summing over 24 of the 30 imaging detectors, excluding the finest subcollimators. The time evolutions of the nonthermal HXR component observed by the two instruments agree well within the error bars of STIX.

For our preliminary analysis of STIX and Fermi/GBM directivity measurements, we selected two flares at moderate intensity, to make sure that pileup effects are not an issue with Fermi/GBM. One of the flares (SOL2021-11-01T01; see Figure 10, bottom row) is seen from almost the same viewing angles for both instruments, and it is used to check that indeed a directivity of 1 is measured. The data is taken from a time when STIX was close to the Earth–Sun line. The viewing angle for both instruments is 57° . The second event (SOL2021-08-28T05; see Figure 10, top row) shows a 30° difference in viewing angles. To simplify the initial analysis, the directivity is determined at the main nonthermal peak of each of the flares. We selected the following simple approach to measure directivity in order to obtain initial results:

1. For each of the Fermi/GBM detectors, a time-dependent background is subtracted by selecting pre- and post-flare time intervals. We then fit the time evolution using a polynomial. SOL2021-11-01 clearly has a time-varying background and a polynomial of order 3 is used, while for SOL2021-08-28 the background is only minimally changing in time and a first-order polynomial represents the background well.

2. For each detector, the GBM spectrum is fitted over the peak time of the nonthermal emission using the Object Spectral Executive (OSPEX software; Schwartz et al. 2002). To keep it simple, we only fit the nonthermal emission, excluding energies below 15 keV that contain thermal counts. The spectral form used in the fitting does not really matter for the initial analysis, as long as the fit represents the data well with evenly distributed residuals and a $\chi^2 < 2$. We use a thermal and a thick-target broken power law. Hence, in this initial analysis, we do not yet fit an albedo component; we simply want to create a fit that represents the data well, to be able to convolve the fitted function in the next step.
3. The STIX spectral response matrix is used to convolve the GBM-derived fit parameters in order to calculate the expected counts in the STIX science energy bins. We use the standard deviation of the results of the individual GBM detectors as a measurement of the accuracy of the expected STIX counts.
4. The ratio of the observed and the GBM-derived STIX counts is then calculated including the error estimates.

The main step that makes our analysis preliminary is the version of the STIX spectral response matrix used. The used

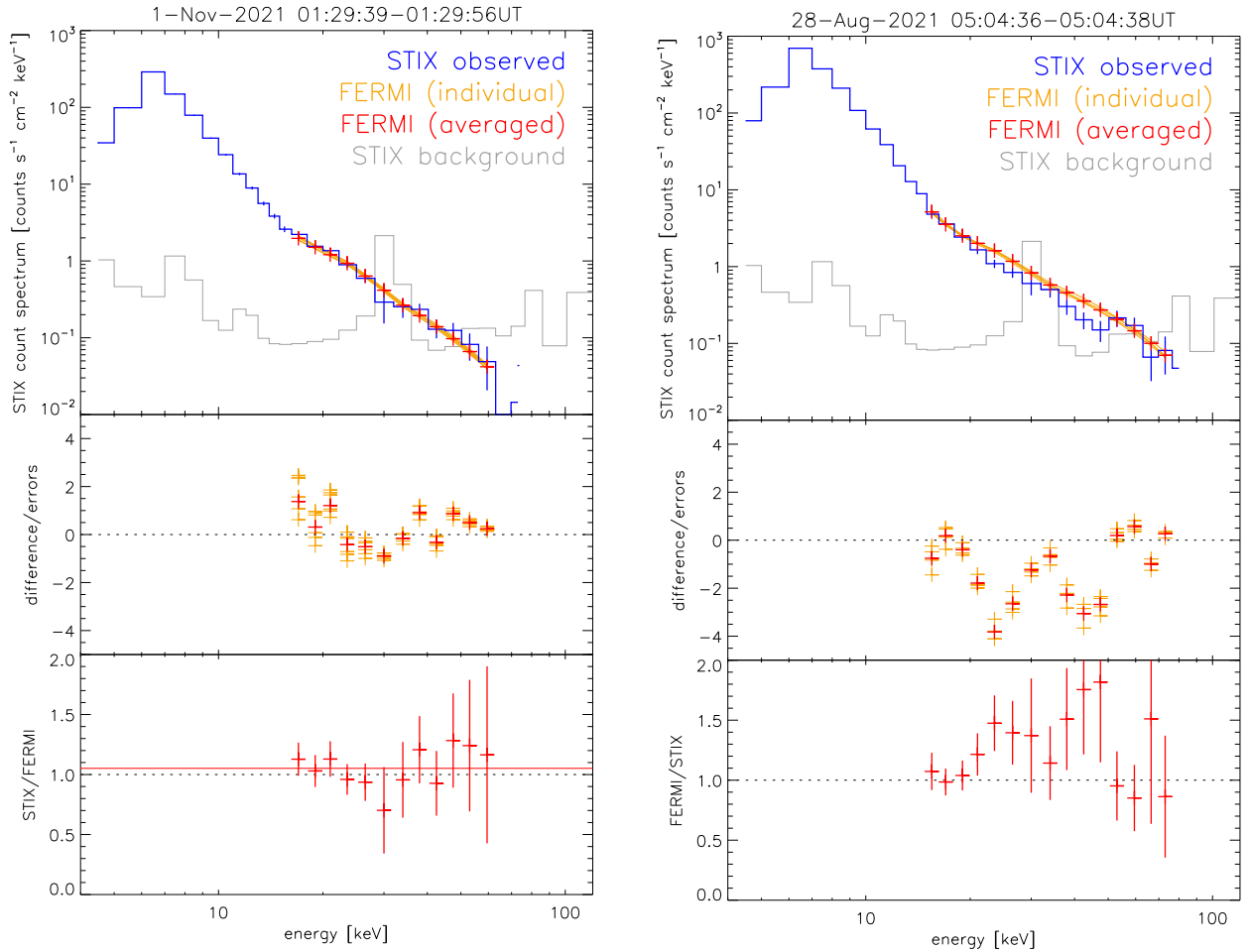


Figure 11. Comparison of the observed HXR directivity determined from Fermi/GBM and STIX observations for two flares: The flare on the left is seen from essentially the same viewing angle (SOL2021-11-01T01), while the flare on the right has a difference in viewing angle of $\sim 30^\circ$ (SOL2021-08-28T05). For SOL2021-11-01T01, we find a directivity close to unity (1.05 ± 0.06), as expected, validating the STIX and Fermi/GBM instrumental calibration. While the individual error bars are large, SOL2021-08-28T05 shows a systematic deviation from a directivity of unity, showing the expected albedo “bump.”

version is from 2023 October and includes the following features:

1. The Energy LookUp Table (Krucker et al. 2020) correction used assumes a constant spectral shape. The spectral shape is obviously not flat. However, the associated uncertainties are on the order of a percent for each individual pixel. As we average over hundreds of pixels, the error is smoothed out, making the approximation of a flat spectrum viable.
2. The livetime correction uses parameters obtained by self-calibration to make the calibration line at 81 keV constant in time during flares. As the reported flares have rather high livetimes (i.e., above 97% for the two events discussed), any further improvement of the livetime calculation will not affect the livetime correction used here.
3. STIX grids are assumed to have sharp edges (i.e., fuzzy grid implementation is not yet used). To minimize this effect, we only use the coarse half of the subcollimators. Estimates suggest that the introduced error is on the order of $\sim 3\%$ at low energies (averaged over the coarse grids), but the error is not yet determined for the energy range relevant here.

4. The detector response matrix is at nominal STIX science bin resolution (i.e., without oversampling in energy).

In any case, the currently used spectral response matrix should be well within the 10% error limit that is desired for directivity measurements (see Section 3.6). As it is difficult to precisely quantify the current shortcomings without implementing associated corrections, here we use our control flare, which is seen from the same viewing angle for both instruments, to showcase the currently available accuracy. The spectral analysis of our test case is shown in Figure 11 (left), and there is indeed good agreement, as expected: the average over all points gives a ratio of 1.05 ± 0.06 . As the event is not particularly strong for STIX, the error bars are rather large above 30 keV. However, the measurements below 30 keV are well constrained. The individual Fermi/GBM detectors give the same result, with a scatter of about 5%. In summary, the current calibration has not yet reached the 5% level for ratio measurements of individual energy bins, but the accuracy is better than 10%.

For SOL2021-08-28T05 (Figure 11, right), a directivity signal is measured. While the error bars at individual energies are rather large, it is clear that the Fermi/GBM detected signal is clearly stronger from ~ 20 to ~ 50 keV, as expected from the

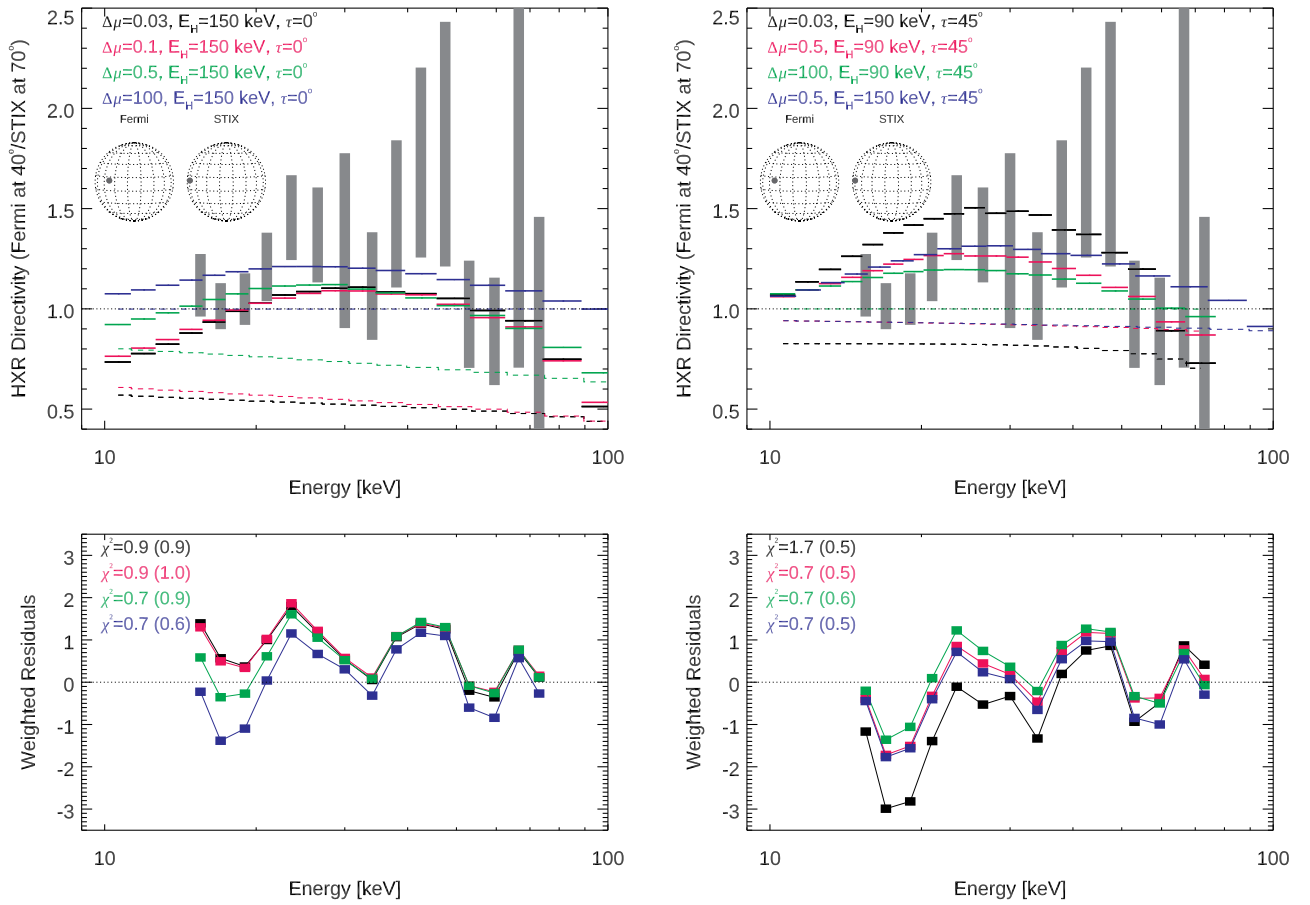


Figure 12. For flare SOL2021-08-28T05, a comparison of the HXR directivity determined from Fermi/GBM and STIX observations with selected simulation runs. Top left: Determined HXR directivity (gray bars) and four simulation curves with varying electron directivities ($\Delta\mu = 0.03$, $\Delta\mu = 0.1$, $\Delta\mu = 0.5$ and $\Delta\mu = 100$) and $E_H = 150$ keV and $\tau = 0^\circ$. Top right: As top left, but for simulation curves with $\tau = 45^\circ$ ($\Phi = 90^\circ$) and different electron directivities ($\Delta\mu = 0.03$, $\Delta\mu = 0.5$ and $\Delta\mu = 100$) and high-energy cutoffs $E_H = 90$ keV and $E_H = 150$ keV. Bottom: The weighted residuals, i.e., (data-model)/(data error) for each simulation shown in the top row, alongside the reduced χ^2 values for all energies and only energies above 23 keV (value in the brackets).

varying importance of albedo. For energies below 20 keV and above 60 keV, directivity is smaller. Below 20 keV, the measurements are becoming consistent with unity. This could be due to the decreasing importance of albedo but also to the increasing contribution of the thermal X-ray flux, which is expected to be isotropic. The error bars at higher energies are very large, but nevertheless a trend is seen toward directivity < 1 compared to what is seen at 30 keV. In the following paragraph, a more detailed comparison with the modeling results from the previous section is discussed.

For SOL2021-08-28T05, we compared the observed HXR directivity with several transport-independent simulations using electron anisotropies of $\Delta\mu = 0.03$, 0.1, 0.5, and 100 (very beamed to isotropic), electron high-energy cutoffs of $E_H = 90$ keV and $E_H = 150$ keV, and a local loop tilt of either $\tau = 0^\circ$ or $\tau = 45^\circ$ (with $\Phi = 90^\circ$). The residuals, calculated as (data-model)/(data error) and resulting reduced χ^2 values, are then used to give an indication of the “goodness of fit.” For a selection of simulation runs, the data–simulation comparison, residuals and χ^2 values are shown in Figure 12. The results of Figure 12 show that the uncertainties of SOL2021-08-28T05 are too large to constrain the individual electron and flare parameters in this flare. The residuals and χ^2 values of all simulation runs are consistent with the data (ranging from $\chi^2 = 0.5$ –1.7), and hence the electron directivity, high-energy

cutoff, and local loop geometry cannot be constrained here. However, at this preliminary stage, the data are already consistent with the modeling outcomes; the expected 20–60 keV “bump” due to X-ray albedo is clearly visible.

5. Summary

The measurement of HXR directivity from X-ray stereoscopy presents us with a prime opportunity for determining the unknown properties of solar flare acceleration, unavailable from X-ray spectra viewed from a single viewpoint. In particular, it elucidates:

1. An electron angular (pitch-angle) distribution related to the acceleration process and coronal transport properties,
2. The highest-energy accelerated electrons related to the acceleration process and local plasma properties, and
3. The dominant magnetic field configuration via the property of “loop tilt.”

The preliminary simulations outlined here can be compared directly with HXR spectroscopy results. In particular, the following observations will help to determine the electron directivity and other properties from HXR directivity.

1. If the HXR directivity at energies outside of 20–50 keV (where the albedo component dominates), in particular at

higher energies, is below 1, then the HXR directivity is suggestive of significant anisotropy (as shown in Figure 5).

2. Knowing how quickly HXR directivity falls to its lowest values at higher energies (>70 keV) helps to constrain the highest-energy X-ray-producing electrons (as shown in Figure 6).
3. Large values of HXR directivity at its peak (≈ 20 – 50 keV) can be suggestive of high values of loop tilt, where the dominant loop direction is away from the local solar vertical direction (as shown in Figure 7).












Our analysis shows the importance of accounting for the X-ray albedo component. For our preliminary stereoscopy study and comparison with simulation, we examined two flares: SOL2021-11-01T01 and SOL2021-08-28T05, observed by both SoLO/STIX and Fermi/GBM. SOL2021-11-01T01 was used to check that a directivity of ~ 1 occurs when spacecraft view the flare at the same viewing angle, with the observation giving an average ratio of 1.05 ± 0.06 . SOL2021-08-28T05 did provide a directivity ratio greater than one, in particular over the dominant albedo energies of 20–50 keV, consistent with the albedo “bump” shown in the simulations. However, SOL2021-08-28T05, with its large uncertainties and small viewing angle difference of $\approx 30^\circ$, is not ideal for directivity studies, and electron and flare parameters could not be constrained in this observation.

As we move into the maximum of solar cycle 25, many more flares will be observed with multiple X-ray instruments, and joint STIX-Fermi/GBM STIX-HXI, STIX-KONUS, and STIX-HEL1OS flare lists are being created. The different detector systems on board these missions have different strengths and difficulties. For example, Fermi/GBM has a relatively large effective area, but pileup issues are severe, in particular for large flares. For HXI, the ~ 7 keV energy resolution is a limiting factor compared to the 1 keV value for STIX, but at the higher energies around ~ 100 keV, accurate measurements are potentially feasible. The PADRE CubeSat launched in late 2025 will make X-ray spectral measurements with the same detectors as STIX, likely providing the most accurate directivity measurements, as systematic errors should be similar and therefore divide out when measuring the directivity. In any case, for each instrument, the accuracy of the absolute flux calibration needs to be carefully established in order to be able to calculate meaningful error bars on the observed directivity. Before quantitative conclusions can be drawn, a study of the systematic uncertainties must be additionally performed by comparing spectra measured by the different detectors from similar viewing angles (i.e., within $\sim 10^\circ$). As the orbit of SoLO has a bias of spending relatively more time close to Earth or on the far side of the Sun, good observing times for directivity measurements with large angular separation are limited to two months around April and October—at least until after 2026, when SoLO will begin to leave the ecliptic. Nevertheless, we expect enough events to perform a statistical study. Finally, after preliminary comparisons, the next modeling steps will include the presence of multiple X-ray sources, the effects of more complex and realistic magnetic configurations, and pitch-angle distributions derived from possible underlying acceleration mechanisms.

Acknowledgments

N.L.S.J. gratefully acknowledges the current financial support from the Science and Technology Facilities Council (STFC) Grant ST/V000764/1. M.S. gratefully acknowledges financial support from a Northumbria University Research Development Fund (RDF) studentship. The authors acknowledge IDL support provided by STFC. All authors are supported by an international team grant “Measuring Solar Flare HXR Directivity using Stereoscopic Observations with SoLO/STIX and X-ray Instrumentation at Earth”¹¹ from the International Space Sciences Institute (ISSI) Bern, Switzerland. Solar Orbiter is a space mission of international collaboration between ESA and NASA, operated by ESA. The STIX instrument is an international collaboration between Switzerland, Poland, France, Czech Republic, Germany, Austria, Ireland, and Italy. A.F.B., H.C., and S.K. are supported by the Swiss National Science Foundation Grant 200021L_189180 for STIX. A.M.V. acknowledges the Austrian Science Fund (FWF): project No. I455-N. Y.S. and F.X. acknowledge the National Natural Science Foundation of China (Grant Nos. 11820101002 and 12333010).

ORCID iDs

Natasha L. S. Jeffrey  <https://orcid.org/0000-0001-6583-1989>
 Säm Krucker  <https://orcid.org/0000-0002-2002-9180>
 Morgan Stores  <https://orcid.org/0000-0002-6060-8048>
 Eduard P. Kontar  <https://orcid.org/0000-0002-8078-0902>
 Pascal Saint-Hilaire  <https://orcid.org/0000-0002-8283-4556>
 Andrea F. Battaglia  <https://orcid.org/0000-0003-4490-7344>
 Laura Hayes  <https://orcid.org/0000-0002-6835-2390>
 Hannah Collier  <https://orcid.org/0000-0001-5592-8023>
 Astrid Veronig  <https://orcid.org/0000-0003-2073-002X>
 Yang Su  <https://orcid.org/0000-0002-4241-9921>
 Fanxiaoyu Xia  <https://orcid.org/0000-0002-2630-4753>

References

- Alaoui, M., & Holman, G. D. 2017, *ApJ*, **851**, 78
 Alaoui, M., Holman, G. D., Allred, J. C., & Eufrazio, R. T. 2021, *ApJ*, **917**, 74
 Alexandrova, O., Chen, C. H. K., Sorriso-Valvo, L., Horbury, T. S., & Bale, S. D. 2013, *SSRv*, **178**, 101
 Aschwanden, M. J., Caspi, A., Cohen, C. M. S., et al. 2017, *ApJ*, **836**, 17
 Bai, T., & Ramaty, R. 1978, *ApJ*, **219**, 705
 Benz, A. O. 2008, *LRSP*, **5**, 1
 Brown, J. C., Emslie, A. G., & Kontar, E. P. 2003, *ApJL*, **595**, L115
 Chen, B., Bastian, T. S., Shen, C., et al. 2015, *Sci*, **350**, 1238
 Dahlin, J. T., Drake, J. F., & Swisdak, M. 2014, *PhPl*, **21**, 092304
 Daughton, W., Roytershteyn, V., Karimabadi, H., et al. 2011, *NatPh*, **7**, 539
 Dickson, E. C. M., & Kontar, E. P. 2013, *SoPh*, **284**, 405
 Drake, J. F., Swisdak, M., Che, H., & Shay, M. A. 2006, *Natur*, **443**, 553
 Emslie, A., Dennis, B., Shih, A., et al. 2012, *ApJ*, **759**, 71
 Emslie, A. G. 1980, *ApJ*, **235**, 1055
 Emslie, A. G., Bradsher, H. L., & McConnell, M. L. 2008, *ApJ*, **674**, 570
 Gardiner, C. W. 1986, *ApOpt*, **25**, 3145
 Gluckstern, R. L., & Hull, M. H. 1953, *PhRv*, **90**, 1030
 Haug, E. 1972, *SoPh*, **25**, 425
 Holman, G. D., Aschwanden, M. J., Aurass, H., et al. 2011, *SSRv*, **159**, 107
 Jeffrey, N. L. S., & Kontar, E. P. 2011, *A&A*, **536**, A93
 Jeffrey, N. L. S., Kontar, E. P., Bian, N. H., & Emslie, A. G. 2014, *ApJ*, **787**, 86
 Jeffrey, N. L. S., Kontar, E. P., & Fletcher, L. 2019, *ApJ*, **880**, 136
 Jeffrey, N. L. S., Saint-Hilaire, P., & Kontar, E. P. 2020, *A&A*, **642**, A79

¹¹ <https://teams.issibern.ch/solarflarexray/team/>

- Kane, S. R., Hurley, K., McTiernan, J. M., et al. 1992, AAS Meeting, [180, 23.07](#)
- Kane, S. R., Hurley, K., McTiernan, J. M., et al. 1998, [ApJ](#), **500**, [1003](#)
- Kašparová, J., Kontar, E. P., & Brown, J. C. 2007, [A&A](#), **466**, [705](#)
- Kirsch, M. G., Briel, U. G., Burrows, D., et al. 2005, [Proc. SPIE](#), **5898**, [22](#)
- Klein, K.-L., & Dalla, S. 2017, [SSRv](#), **212**, [1107](#)
- Knight, J. W., & Sturrock, P. A. 1977, [ApJ](#), **218**, [306](#)
- Kontar, E., Brown, J., Emslie, A., et al. 2011, [SSRv](#), **159**, [301](#)
- Kontar, E., Perez, J., Harra, L., et al. 2017, [PhRvL](#), **118**, [155101](#)
- Kontar, E. P., Bian, N. H., Emslie, A. G., & Vilmer, N. 2014, [ApJ](#), **780**, [176](#)
- Kontar, E. P., & Brown, J. C. 2006, [ApJL](#), **653**, [L149](#)
- Kontar, E. P., Jeffrey, N. L. S., Emslie, A. G., & Bian, N. H. 2015, [ApJ](#), **809**, [35](#)
- Kontar, E. P., Jeffrey, N. L. S., & Emslie, A. G. 2019, [ApJ](#), **871**, [225](#)
- Krucker, S., Hurford, G. J., Grimm, O., et al. 2020, [A&A](#), **642**, [A15](#)
- Krucker, S., Hurford, G. J., Su, Y., & Gan, W.-Q. 2019, [RAA](#), **19**, [167](#)
- Krucker, S., Kontar, E. P., Christe, S., & Lin, R. P. 2007, [ApJL](#), **663**, [L109](#)
- Larosa, T. N., & Moore, R. L. 1993, [ApJ](#), **418**, [912](#)
- Leach, J., & Petrosian, V. 1983, [ApJ](#), **269**, [715](#)
- Lemen, J. R., Title, A. M., Akin, D. J., et al. 2012, [SoPh](#), **275**, [17](#)
- Lin, R. P., Dennis, B. R., Hurford, G. J., et al. 2002, [SoPh](#), **210**, [3](#)
- McConnell, M. L., Smith, D. M., Emslie, A. G., et al. 2004, [AdSpR](#), **34**, [462](#)
- Meegan, C., Lichti, G., Bhat, P. N., et al. 2009, [ApJ](#), **702**, [791](#)
- Melrose, D. B. 1994, [ApJS](#), **90**, [623](#)
- Miller, J. A., Larosa, T. N., & Moore, R. L. 1996, [ApJ](#), **461**, [445](#)
- Müller, D., Cyr, O. C., St., Zouganelis, I., et al. 2020, [A&A](#), **642**, [A1](#)
- Musset, S., Kontar, E. P., & Vilmer, N. 2018, [A&A](#), **610**, [A6](#)
- Parker, E. N. 1957, [JGR](#), **62**, [509](#)
- Petrosian, V. 2012, [SSRv](#), **173**, [535](#)
- Petrosian, V., & Donaghy, T. Q. 1999, [ApJ](#), **527**, [945](#)
- Priest, E., & Forbes, T. 2002, [A&ARv](#), **10**, [313](#)
- Schwartz, R. A., Csillaghy, A., Tolbert, A. K., et al. 2002, [SoPh](#), **210**, [165](#)
- Stores, M., Jeffrey, N. L. S., & McLaughlin, J. A. 2023, [ApJ](#), **946**, [53](#)
- Strauss, R. D. T., & Effenberger, F. 2017, [SSRv](#), **212**, [151](#)
- Su, Y., Liu, W., Li, Y.-P., et al. 2019, [RAA](#), **19**, [163](#)
- Su, Y., Veronig, A. M., Holman, G. D., et al. 2013, [NatPh](#), **9**, [489](#)
- Suarez-Garcia, E., Hajdas, W., Wigger, C., et al. 2006, [SoPh](#), **239**, [149](#)
- Sweet, P. A. 1958, in IAU Symp. 6, Electromagnetic Phenomena in Cosmical Physics, ed. B. Lehnert (Cambridge: Cambridge Univ. Press), [123](#)
- Tindo, I. P., Ivanov, V. D., Mandel'stam, S. L., & Shuryghin, A. I. 1970, [SoPh](#), **14**, [204](#)
- Vlahos, L., Pisokas, T., Isliker, H., Tsiolis, V., & Anastasiadis, A. 2016, [ApJL](#), **827**, [L3](#)
- Warmuth, A., & Mann, G. 2016, [A&A](#), **588**, [A116](#)
- Zhang, Z., Chen, D.-Y., Wu, J., et al. 2019, [RAA](#), **19**, [160](#)
- Zharkova, V. V., & Gordovskyy, M. 2006, [ApJ](#), **651**, [553](#)